Faraday Discussions

Bio-inspired gas sensing: boosting performance with sensor optimization guided by "machine learning"

Journal:	*Faraday Discussions*
Manuscript ID	FD-ART-03-2020-000035.R1
Article Type:	Paper
Date Submitted by the Author:	05-May-2020
Complete List of Authors:	Potyrailo, Radislav; General Electric, Global Research Center; Brewer, Joleyn; GE Global Research, Cheng, Baokai; GE Global Research Carpenter, Michael; SUNY Polytechnic Institute, Albany NY, USA Houlihan, Nora; SUNY Polytechnic Institute, Albany NY, USA Kolmakov, Andrei; NIST, PML

Bio-inspired gas sensing: boosting performance with sensor optimization guided by "machine learning"

R. A. Potyrailo,[a*] J. Brewer,[a] B. Cheng,[a] M. A. Carpenter,[b] N. Houlihan,[b] and A. Kolmakov[c]

[a] GE Research, Niskayuna NY, USA

[b] SUNY Polytechnic Institute, Albany NY, USA

[c] National Institute of Standards and Technology, Gaithersburg, MD, USA

Prepared for submission to *Faraday Discussions*

---

*Corresponding author: R. A. Potyrailo, email: potyrailo@ge.com

Abstract

The performance of existing gas sensors often degrades in the field conditions because of the loss of the measurement accuracy in the presence of interferences. Thus, new sensing approaches are required with improved sensor selectivity. We are developing a new generation of gas sensors, known as multivariable sensors, that have several independent responses for multi-gas detection with a single sensor. In this study, we analyze capabilities of natural and fabricated photonic three-dimensional (3-D) nanostructures as sensors for detection of different gaseous species such as vapors and non-condensable gases. We employed bare *Morpho* butterfly wing scales to control their gas selectivity with different illumination angles. Next, we chemically functionalized *Morpho* butterfly wing scales with a fluorinated silane to boost the response of such nanostructure to vapors of interest and to suppress the response to ambient humidity. Further, we followed our earlier developed design rules of sensing nanostructures and fabricated bioinspired inorganic 3-D nanostructures to achieve a functionality beyond natural *Morpho* scales. These fabricated nanostructures have embedded catalytically active gold nanoparticles to operate at high temperatures of ≈ 300 ^{o}C for detection of gases for solid oxide fuel cell (SOFC) applications. Our performance advances in detection of multiple gaseous species with specific nanostructure designs were achieved by coupling spectral responses of these nanostructures with machine learning (a.k.a. multivariate analysis, chemometrics) tools. Our newly acquired knowledge from studies of these natural and fabricated inorganic nanostructures coupled with machine learning data analytics allowed us to advance our design rules of sensing nanostructures toward needed gas selectivity for numerous gas monitoring scenarios at room and high temperatures for industrial, environmental, and other applications.

Keywords: sensing, solid oxide fuel cell, photonic, nanostructure, bioinspired

1. Introduction

Accurate detection of gases of interest is demanded in contemporary applications ranging from urban pollution and industrial safety to medical diagnostics, process control, and homeland protection.[1] Existing sensors often have their performance degraded in field conditions because of the loss of the measurement accuracy in the presence of interferences.[2, 3] Therefore, in demanding applications, conventional analytical instruments are preferred.[4-7] Unfortunately, these instruments are inconvenient in the field even with reduced carrier gas, vacuum, or power demands,[8] but are an unavoidable alternative to existing sensors.

Thus, innovative approaches are required to improve sensor selectivity that will allow accurate detection of gases of interest in the background of other gases. Recently, a new generation of gas sensors, known as multivariable sensors, has emerged with a fundamentally different perspective for sensing to eliminate limitations of existing sensors[9-18] and conventional sensor arrays with up to 2^{16} sensing elements in the array.[19-25] The field of sensor arrays (also known as electronic noses) has matured to an understanding of their applicability and limitations outside controlled laboratory conditions (e.g., an uncorrelated drift of each sensor in an array, inability to provide accurate quantitation of multiple vapors in their mixtures, and inability to operate in the presence of high levels of known and unknown interferences).[18]

Multivariable sensors (also known as intelligent,[26] multiparameter,[27] high-order,[28] or multidimensional signatures[29] sensors, virtual multisensor systems,[30] or virtual sensor arrays[31]) provide several partially or fully independent responses from a sensor.[9-18] Among different designs of multivariable sensors, we discovered that a *Morpho* butterfly photonic 3-D nanostructure provided an unusual high selectivity of vapor sensing.[32] These initial results

inspired our studies to understand the origin of such gas selectivity[33] and to implement such knowledge in fabricated artificial bio-inspired photonic nanostructures.[34]

In this study, we analyze effects of different gaseous species such as vapors and non-condensable gases on sensing performance of natural and fabricated photonic 3-D nanostructures. To control gas selectivity, we studied effects of different illumination angles and chemical functionalization of bare *Morpho* butterfly wing scales. We followed our design rules of sensing nanostructures[34] and fabricated bioinspired inorganic 3-D nanostructures to achieve a functionality beyond natural *Morpho* scales. These nanostructures have embedded catalytically active gold nanoparticles to operate at high temperatures for detection of H_2 and CO gases. Detection of these gases in the presence of numerous interferences such as CO_2, CH_4, and H_2O is important for solid oxide fuel cell (SOFC) applications.[35-38] Our performance advances in detection of multiple gaseous species with specific nanostructure designs were accomplished by coupling the optical spectral responses of these nanostructures with machine learning tools. Our new acquired knowledge from studies of these natural and fabricated inorganic nanostructures coupled with machine learning data analytics allowed us to advance our design rules of sensing nanostructures toward needed gas selectivity for numerous gas monitoring scenarios.

2. Multivariable gas sensors as next generation analytical instruments

2.1. Principles of multivariable gas sensors

Modern conventional gas sensors (**Figure 1A**) were not designed to differentiate gases[39-43] leading to the need of sensor arrays.[19, 44] Conventional gas sensors perform best when the levels of gases of interest are high and when the gas of interest swamps others.[3] Thus, conventional single-output gas sensors respond not only to a gas of interest but also to many other gases (**Figure 1B**). To discriminate gaseous species, other design principles are more

appropriate with one or more independent measurement variables (outputs) implemented in a single instrument. Traditional mature analytical instruments are based on these design principles (**Figure 1C**). Their high performance capabilities are provided by independent variables in their outputs, e.g. retention time in gas chromatography and mass-to-charge ratio in mass spectrometry detectors, drift time in ion-mobility or wavelengths in infrared detectors. Independent outputs allow selective detection of different gases of interest and rejection of interferences (**Figure 1D**).

Diverse designs of multivariable sensors have the common goal – to overcome the gas cross-sensitivity of existing single-output sensors. Multivariable sensors are built following the design rules of traditional instruments to have independent variables but to provide different types of such variables for multi-gas detection. General design criteria for multivariable sensors involve (1) a sensing material structure with diverse responses to different gases, (2) a multivariable transduction methodology to provide independent outputs and to recognize these different gas responses, (3) excitation conditions of the multivariable sensor to maximize these different gas responses, and (4) data analytics ("machine learning") to provide multianalyte quantitation, rejection of interferences, and drift minimization.

Over the recent years, multivariable gas sensors were demonstrated based on diverse principles including multi-output field-effect transistors, broad-range impedance spectroscopy, radio frequency and microwave resonators, photonic nanostructures as well as electromechanical devices such as tuning forks, thickness shear mode devices, and acoustic-wave devices.[18] All multivariable sensors form independent variables in sensor response to deliver sensor performance similar to traditional analytical instruments (**Figure 1D**) but with reduced size and power, for example by using bio-inspired photonic nanostructures (**Figure 1E**). Such technical

solution eliminates the size limitations of traditional analytical instruments and allows miniaturization, leading to previously unachievable deployments.

2.2. The role of "machine learning" tools in multivariable gas sensors

Tools for multivariate analysis of data from multivariable sensors can be adapted from those used for sensor arrays (**Table 1**)[18] and other areas of science.[45, 46] The capabilities of multivariable sensors are determined by the number of independent outputs (also known as dispersion, dimensionality, or order)[18] generated by the sensor upon the data analysis. With the increase of the sensor dispersion, multivariable gas sensors discriminate known and uncalibrated-for interferences and individual gases in complex mixtures.[18, 47, 48]

While many of multivariable sensors have only 2-D dispersion,[49-64] there is a growing number of multivariable sensors with higher dispersion. Recent examples of 3- to 4-D dispersion include radio frequency and optical sensors as well as field-effect transistors.[13, 18, 29, 31-34, 65-78] Multivariable photonic sensors based on bio-inspired structural designs demonstrated 3- to 4-D dispersion[18, 32-34, 65, 70-78] in detection of individual condensable vapors and their mixtures.

2.3. General design rules of structure-based photonic multivariable gas sensors

Structure-based photonic sensors are comprised of units that are comparable with the wavelength of interrogation light.[79-81] Such sensors often operate based on single-output vapor quantitation principles such as detection of wavelength shift of the resonance peak[82-86] or detection of signal magnitude change at a single wavelength.[87] Monitoring of multiple gases of interest using these approaches requires traditional sensor arrays.[83, 88, 89] However, these physical structures also allow multivariable performance of photonic sensors.[32, 33, 65, 90, 91 92, 93]

A tree-like photonic nanostructure of microscopic scales that produces iridescence of tropical *Morpho* butterflies was found to be attractive for sensing of volatiles[32] because of its open-air architecture that allows volatiles to interact with all its regions such as ridges, lamella, and microribs (**Figure 1E**). From the initial[32] and detailed[33] studies of the multi-vapor-response of natural *Morpho* scales, numerical analysis of optical effects from multiple vapors,[34] and fabrication of bio-inspired nanostructures using modern lithographic tools,[34, 94-97] we have developed general design rules of structure-based photonic multivariable sensors for condensable vapors and non-condensable gases that involve physical and chemical design criteria.[34, 94-97]

Physical design is achieved by the nanostructure geometry and physical mechanisms of light loss in the nanostructure. Geometry of the nanostructure involves interferometric lamella and their supporting ridges resulting in a highly ordered hierarchical photonic design also contributing to the diffraction effects from the nanostructure. Vertical ridges serve as spacers to provide a high refractive index contrast (air gap) between lamella and to induce the ability for gaseous species to interact with all the regions of the nanostructure. A small controlled loss of light in the nanostructure (by material extinction and/or scattering) results in a desired enhancement of diversity of reflectance spectra of localized gas-nanostructure interactions. This loss gives rise to distinct signatures of reflectance spectra that are induced by the optical attenuation when light propagates between the top and bottom regions of the lamella stack.

Chemical design uses spatially controlled functionalization of the nanostructure to promote distinct interactions of diverse gaseous species within the nanostructure. Diverse functionality can be also introduced into the horizontal and vertical regions of the nanostructures. The availability of the broad range of materials allows tuning the response selectivity of a given nanostructure across the wide range of gaseous species and operating temperatures.

In our work, we are optimizing performance of multivariable sensors by refining their material, structural, and excitation characteristics based on the results of multivariate ("machine learning") analysis. We perform the iterative multivariate machine learning analysis of system performance in each iteration (**Figure 2**). Our examples of sensing parameters for their optimization include sensitivity, selectivity, response/recovery times, dynamic range, and stability. In this Discussion, we present our results on sensitivity and selectivity of the system.

3. Experimental

In this study, we evaluated responses of natural and fabricated nanostructures to diverse vapors and non-condensable gases in laboratory conditions. Optical measurements with all samples were performed in reflectance mode[32-34, 94, 97] as schematically depicted in **Figure 1E**. The illumination angle was at 45^{o} unless specified otherwise. Conventionally, when spectral changes are small, the differential reflectance spectral response $\Delta R(\lambda)$ is measured in traditional optical instruments[98] and in gas sensors.[32-34] The differential reflectance spectral response $\Delta R(\lambda)$ of photonic 3-D nanostructures is given by

$$\Delta R(\lambda) = R(\lambda)/R_0(\lambda), \qquad \text{(eq.1)}$$

where $R(\lambda)$ is the spectrum of the sensing nanostructure upon exposure to gaseous species of interest and $R_0(\lambda)$ is the spectrum of the sensing nanostructure upon exposure to a carrier gas (a blank). Thus, the common features in the two spectra before and during gas exposure cancel and the $\Delta R(\lambda)$ spectrum accentuates the subtle differences due to gas response.

We used systems to operate with non-hazardous gas mixtures or explosive and toxic gases.[94, 97] Measurements with natural *Morpho* butterfly nanostructures were performed at room temperature using air as a blank carrier gas with different concentrations of condensable vapors

ranging from 0.09 to 0.5 P/P_0, where P is vapor partial pressure and P_0 is the saturated vapor pressure. Measurements with the fabricated 3-D photonic nanostructures were performed with different non-condensable gases using nitrogen as a blank carrier gas using a built-in-house gas flow cell with an integrated heater to bring a sensing nanostructure sample to ≈ 300 °C.[97]

To investigate computationally the gas-selectivity control in 3-D nanostructures with different light illumination angles, we applied the finite-difference time domain (FDTD) computational method. We simulated the spectral response of the 3-D nanostructure using a periodic boundary condition and a perfect matched layer. Simulations were done in 2-D to improve speed. The excitation plane was set above the top lamella of the nanostructure with the monitor plane above the excitation plane. The excitation wave was pointed downwards at a chosen angle. The reflectance intensity was obtained from the power received at the monitor plane. The spectra upon exposures to vapors were the ratio of the received optical power at the monitor plane to the optical power of the excitation wave. For visualization, we further processed spectra using eq. 1.

From the available machine leaning tools (see **Table 1**) in this study we report results of using Principal component analysis (PCA). It is the most popular tool in data analysis in multivariable sensors[17, 18, 47, 48, 99, 100] and sensor arrays.[101, 102] With PCA we were reducing data sets of $\Delta R(\lambda)$ spectra from different gaseous species and their different concentrations or measurement angles for easier interpretation by calculating orthogonal principal components (PCs) oriented in the direction of the maximum variance within each data set. The spectra for analysis were from the equilibrated responses to gaseous species and the blank.

4. Results and discussion

4.1. 3-D nanostructured materials

For gas-phase sensing reported in this study, we utilized natural *Morpho* butterfly scales and fabricated nanostructures. *Morpho* butterfly scales were functionalized with trimethoxy(nonafluorohexyl)silane using vapor deposition.[34] Bare and functionalized *Morpho* butterfly nanostructures were tested for their responses to diverse and closely related vapors. Fabrication of 3-D bio-inspired nanostructures was performed per design rules developed earlier for condensable vapors and refined for non-condensable gases (see Section 2.3). The nanostructures were fabricated using conventional photolithography and chemical etching forming several layers of horizontal lamella supported by the vertical ridge.[34, 94-97] All materials in these nanostructures were inorganic and included catalytic metal nanoparticles (5 to 50 nm in diameter) and metal-oxide capping layers on nanoparticles to promote the reactions with gases of interest.[68, 103] Results reported in this study for H_2 and CO analyte gases were achieved using fabricated inorganic nanostructures with variable size catalytic metal nanoparticles capped with a metal-oxide ceria layer. Examples of electron micrographs of 3-D nanostructures illustrate our designs with gold metal nanoparticles (**Figure 3**). Examples of samples of sensing nanostructures are presented in **Figure 4**. Our work is in progress toward optimization of the fabrication conditions to achieve desired nanostructure geometries and their functionalization control.

4.2. Experimental gas-selectivity control with light illumination angle

In our initial experiments of responses of bare natural *Morpho* nanostructures to three vapors such as water, methanol, and ethanol,[32] we observed that the diversity of spectral response to different vapors was dependent on the illumination angle. In this study, we explored

this effect in a quantitative detail with three vapors of diverse chemical families such as water, chloroform, and dimethylformamide.

We performed vapor exposures at three illumination angles of 20°, 40°, and 60° measured from the normal to the nanostructure surface. For the initial visual interpretation, **Figure 5A-C** compare $\Delta R(\lambda)$ spectra from these vapors. At a small illumination angle of 20°, the $\Delta R(\lambda)$ spectra of three vapors were very similar. The differences in $\Delta R(\lambda)$ spectra were becoming more significant at 40° and 60°. For the more quantitative interpretation, **Figure 5D** illustrates the PCA scores plot of the first two PCs where we observed two interesting features. First, the angular spread between the response directions of the same sensing nanostructure to three vapors was increasing from 20 ° to 40° and to 60°. Second, the relative magnitudes of the responses were decreasing from 20 ° to 40° and to 60°. Thus, results of machine learning analysis demonstrated a trade-off between the strongest response magnitude and the best discrimination between vapors as controlled by the implemented illumination angle.

4.3. Numerical analysis of gas-selectivity control with light illumination angle

To investigate the gas-selectivity control in 3-D nanostructures with different light illumination angles, we applied the FDTD method that provides a direct integration of Maxwell's time-dependent equations and is a popular tool for simulations of photonic nanostructured gas sensors.[104-106] We performed simulations of effects of different vapors and their concentrations using a nanostructure with four lamella and utilized the values from our prior studies[34] of variable refractive index (n = 1.3, 1.4, 1.5, and 1.6) and variable thickness (d = 5 nm, 10 nm, and 15 nm) of the adsorbed vapors. Concentrations of vapors were related to

condensed liquid layers of thickness *d* = 5 nm, 10 nm, and 15 nm as formed on the nanostructure, detailed earlier.[33, 34] Adsorption of model vapors increased the effective refractive index of the sensor by replacing a fraction of air by a fraction of a liquid analyte with its gas-phase concentration-dependent thickness. Thus, we simulated vapor concentrations as related to liquid layers of different thickness *d* formed on the nanostructure.[33, 34]

Examples of the planar electromagnetic field that interacts with the 3-D sensing nanostructure at different angles such as 0^o, 30^o, and 60^o from the normal to the substrate of the nanostructure are illustrated in the top plots of **Figure 6A-C**. These results show that diverse illumination angles created the electromagnetic field that interacted with the 3-D nanostructure with different symmetry. The simulated $\Delta R(\lambda)$ spectra for three illumination angles are presented in the middle plots of **Figure 6A-C**. The scores plots of the built PCA models for each of the sets of the simulated $\Delta R(\lambda)$ spectra are depicted in the bottom plots of **Figure 6A-C**. These PCA scores plots depict that four model vapors represented by the four refractive indices used for the adsorbate layer (n = 1.3, 1.4, 1.5, and 1.6) at their three concentrations represented by the adsorbate layer of thickness d = 5 nm, 10 nm, and 15 nm distinctly affected the reflectance spectra producing clearly resolved four arms in the PCA response.

The contributions for the first three principal components as a function of the illumination angle are presented in **Figure 6D**. For the largest diversity in sensor response, the contributions of the higher principal components are desired to be as high as possible.[18] From these simulation results we observed that there was a maximum in the contribution of PC3 and a corresponding minimum in the contribution of PC1 at a 30^o-illumination angle. In future, we plan to use FDTD modeling also as a rapid structure-screening tool to assess the gas

selectivity and the effects of fabrication imperfections on sensing performance of our structures.

4.4. Control of discrimination of multiple vapors by functionalization of *Morpho* scales

To explore our ability to control discrimination of multiple vapors, we utilized natural *Morpho* butterfly scales and functionalized them with trimethoxy(nonafluorohexyl)silane. Such functionalization of natural *Morpho* butterfly nanostructures with a volatile silane was selected to enhance diversity of the response to different vapors.[107-109] We selected vapors of water and the first nine linear alcohols such as methanol, ethanol, 1-propanol, 1-butanol, 1-pentanol, 1- hexanol, 1-heptanol, 1-octanol, and 1-nonanol, with four concentrations of each vapor.

Spectral responses $\Delta R(\lambda)$ of bare and functionalized *Morpho* butterfly nanostructures to ten vapors are compared in **Figure 7**. Upon visual inspection, we had three observations about $\Delta R(\lambda)$ spectra of the functionalized versus bare nanostructures. First, the overall response magnitude was higher. Second, the response magnitude to water vapor was suppressed. Third, there was a pronounced tail in spectral response at longer wavelengths, perhaps due to wavelength-dependent scatter from the silane-functionalized nanostructure.

A comparison of dynamic responses of bare and functionalized *Morpho* butterfly nanostructures to ten vapors is depicted in **Figure 8A,B.** These responses are illustrated with two replicates at 550 nm and 620 nm, which are the maxima of the $\Delta R(\lambda)$ spectra of the bare and functionalized *Morpho* nanostructures, respectively. Each vapor was presented to the

nanostructures at four concentrations of 0.09, 0.13, 0.18, and 0.22 P/P_0. To reduce effects of the exposure history and to speed up the recovery time of the *Morpho* wing sample to its baseline, a hydration step between switching to different vapors was used (see **Figure 8C** for zoomed-in display). The hydration step was done by exposing the sample to water vapor at 0.35 P/P_0.[33] From dynamic data, we see that upon fluorosilane functionalization, the response magnitude to water vapor was reduced by ≈ 1.5 fold. **Figure 8C** compares the sensitivity of the *Morpho* butterfly nanostructure to alcohols ranging from 1-propanol to 1-nonanol (vapors 4 - 10) before and after functionalization. These alcohols were previously not resolved using bare *Morpho* scales.[33] The sensitivity to these alcohols was enhanced by 4 to 7.5 fold upon functionalization.

To assess the ability to discriminate between water and nine alcohol vapors, we analyzed the $\Delta R(\lambda)$ spectra using PCA. **Figure 9A-B** depict results of discrimination of ten vapors with a bare *Morpho* nanostructure by plotting the same 3-D scores plot at different angles for better visualization. This data illustrate that the bare nanostructure discriminated well water, methanol, and ethanol vapors, similar to prior results with these vapors[32, 33] but the responses to other alcohol vapors were too close to each other to be discriminated. However, upon chemical functionalization, the *Morpho* nanostructure discriminated all ten vapors. **Figure 9C-D** present the PCA scores plot at different angles to highlight this discrimination ability. Thus, an appropriate chemical functionalization of natural *Morpho* butterfly nanostructure enhanced the response to vapors of interest by up to 7.5 fold and reduced humidity response by ≈ 1.5 fold.

4.5. Response of fabricated photonic 3-D nanostructures to H_2 and CO gases

For H_2 and CO sensing for SOFC applications,[35-38] we fabricated 3-D nanostructures with a ridge of SiN_x material, lamella of SiO_2 material, and gold nanoparticles embedded between the

base and capping ceria layers. The goal of these tests was to evaluate response diversity of the nanostructures to H_2 and CO gases and to assess the linearity of the response to H_2 and CO.

Measurements of nanostructure responses to H_2 and CO were performed with exposures to H_2 gas at 4 %, 8 %, and 11%, followed by exposures to CO gas at 6 %, 13 %, and 19%. The differential reflectance spectra $\Delta R(\lambda)$ of these responses are presented in **Figure 10.** The key aspect of the these spectra is in the pronounced effect of the gold nanoparticles that resulted in the plasmonic signature of the nanostructure between 640 nm to 720 nm.

Results of replicate (n = 2) measurements of nanostructure responses to H_2 and CO gases are depicted in **Figure 11** at four exemplary wavelengths. We selected these wavelengths for the response visualization to highlight two important observations. First, the response magnitude followed the increasing concentrations of H_2 and CO but with some non-linearity. Second, the relative magnitudes of the response to H_2 and CO were wavelength-dependent. For example, the relative magnitudes of the responses to the highest tested concentrations of H_2 and CO gases were in the range from 3:1 to 1.5:1 as shown in **Figure 11** at four exemplary wavelengths.

To assess the ability to discriminate between H_2 and CO, we analyzed $\Delta R(\lambda)$ spectra of the nanostructure using PCA. The scores plot shown in **Figure 12** illustrates the ability to discriminate these gases. Our next steps are to optimize the nanostructure design by increasing the length of the lamella and by functionalization of these extended-length lamella with gold nanoparticles of different size. Such geometry will enhance the response magnitude and the discrimination between H_2 and CO under different test conditions.[68, 97, 103]

4.6. Elimination of effects of CH_4, CO_2, and H_2O in determination of H_2 and CO using fabricated photonic 3-D nanostructures

We applied our methodology of fabrication of 3-D nanostructures to the initial demonstration of elimination of effects of interfering gases such as CH_4, CO_2, and H_2O. These gases were identified as interferences in detection of H_2 and CO for SOFC applications.[35-38] In these experiments for selective determination of H_2 and CO we used our nanostructure design with gold nanoparticles of different size. Concentrations of H_2 and CO were 12.5 %, 25 %, and 37.5%. The CO_2 and CH_4 interferents were at 37.5 %. The H_2O vapor interferent was at 30 % RH. The differential reflectance $\Delta R(\lambda)$ spectra of H_2 and CO are compared with CH_4, CO_2, and H_2O interferences in **Figure 13** depicting their significant differences.

An example of a dynamic response of the nanostructure at 950 nm upon exposure to fives gases with three replicates is illustrated in **Figure 14**. Responses to H_2 and CO were always at least 2 to 3 times stronger versus CH_4, CO_2, and H_2O. Further, the difference in responses at multiple wavelengths (see **Figure 13**) allowed us to reject the effects from CH_4, CO_2, and H_2O by performing multivariable spectral analysis. The PCA scores plots present results as the first three PCs (**Figure 15A**) and as the first two PCs and PC4 (**Figure 15B**) to illustrate a 4-D dispersion of the response. These PCA scores plots showed that the nanostructure discriminated between the H_2 and CO gases of interest and three interferences CH_4, CO_2, and H_2O.

5. Conclusions

At present, for detection of gaseous species two classes of detectors exist with fundamentally different design principles. *One such class of detectors* is single-output sensors that are miniature, low power, and cost-attractive devices. The single-output design principles of such sensors were contemplated last century to serve the needs of detection of expected gases of interest assuming that the responses to interferences are not of a concern. For detection of gaseous chemicals of interest for myriad of contemporary applications, responses of such single-

output detectors to gaseous chemicals of interest and practical interferences become un-distinguishable, decreasing the value of these sensors. *Another class of detectors* is traditional analytical instruments designed with multiple outputs to serve in conditions with expected known and unknown interferences. Unfortunately, design principles of traditional analytical instruments do not allow to operate with power, size, and cost that are comparable to those of single-output sensors.

Our bio-inspired photonic sensing nanostructures that are under development with the most recent results demonstrated here, share the mathematical principles of multiple outputs with traditional analytical instruments but without their large power, size, and cost limitations. Per design, bio-inspired photonic sensing nanostructures provide such capabilities by their nanostructured features, chemical functionalization, and excitation principles. Machine learning tools allow the analysis of the multivariate data and the relation of the weighted outputs to the concentrations of one or more gaseous species of interest.

Our work is in progress to advance our sensing designs to operate in conditions with known and unknown interferences by implementing nanostructures with enhanced spectral diversity of responses to gaseous species of interest and interferences. We expect that in detection of mixtures for SOFC and other applications, we may face challenges that include the relative reactivity of different gases with the sensing surface and the ability to quantify three, four, and more gases with a single nanostructure design. We are solving these challenges by optimization of our multivariable sensing designs by refining the material, structural, and excitation characteristics of the sensing system via the iterative multivariate machine learning analysis of system performance. This systematic reduction of technical risks will facilitate transition of this scientifically innovative sensing technology to practice.

Acknowledgments

We are thankful for the initial fruitful discussions with V. Greanya at the Defense Advanced Research Projects Agency (DARPA) and her visionary insights on exquisite performance capabilities of bio-inspired photonics for demanding applications. We are thankful for the fruitful discussions with J. Abo-Shaeer at DARPA for his insights in relating the fundamental aspects of bio-inspired photonics to its practical implementations. We are thankful for the fruitful discussions with Steven Markovich and Venkat K. Venkataraman at U.S. Department of Energy for the key insights in relating the gas-sensing performance aspects of bio-inspired photonic sensors to their implementations for SOFC applications. We would like to thank S. Duclos, J. Freer, and B. Bewlay at General Electric (GE) Research for providing cost-share support. Initial fundamental aspects of this work on detection of diverse volatiles with natural and bio-inspired nanostructures were supported from DARPA Contract W911NF-10-C-0069. This work has been further supported from U.S. Department of Energy, National Energy Technology Laboratory Cooperative Agreements FE0027918 and DE-FE0031653 for detection of gases for SOFC applications. The findings and conclusions in this report should not be interpreted to represent any determination or policy of the U.S. Department of Defense and the U.S. Department of Energy. The content of the paper does not necessarily reflect the position or the policy of the US Government. Mention of any commercial product does not imply endorsement.

Table 1. Examples of typical machine learning (a.k.a. multivariate analysis, chemometrics) tools for data analysis of multivariable sensors.[18]

Algorithm	Description
Principal component analysis (PCA)	Unsupervised algorithm that reduces a multidimensional data set for its easier interpretation by calculating orthogonal principal components (PCs) oriented in the direction of the maximum variance within the data set. The first PC contains the highest degree of variance, and other PCs follow in the order of decreasing variance. Thus, PCA concentrates the most significant characteristics (variance) of the data into a lower dimensional space.
Discriminant Analysis (DA)	Models the difference between the classes of data and maximizes the ratio of between-class variance to the within-class variance. Requires an input of distinction between independent variables and dependent variables.
Artificial Neural Network (ANN)	A system of a large number of simple highly interconnected processing elements ("neurons") that exchange messages between each other to process information by their dynamic state response to external inputs. The connections have numeric weights that can be tuned based on experience, making neural nets adaptive to inputs and capable of learning.
Hierarchical cluster analysis (HCA)	Classifies samples using a dendrogram representation. Often, a Ward's method is applied that shows the Euclidean distance between the samples. The Ward's method is a minimum variance method, which takes into consideration the minimum amount of variance between the samples and gases (analyte and interferents) to define a cluster.
Support Vector Machines (SVM)	Supervised learning models with associated learning algorithms that analyze data and recognize patterns, used for classification, regression analysis, and outliers detection by finding the decision hyperplane that maximizes the margin between the classes. The vectors (cases) that define the decision hyperplane are the support vectors.
Independent Component Analysis (ICA)	Separates a multivariate signal into additive subcomponents by assuming that the subcomponents are statistically mutually independent non-Gaussian signals. A powerful technique for revealing hidden factors that underlie sets of random variables, measurements, or signals.
Partial least squares (PLS) regression	Determines correlations between the independent variables and the sensor response by finding the direction in the multidimensional space of the sensor response that explains the maximum variance for the independent variables. The key outputs of the developed multivariate models are residual errors of calibration and cross-validation.
Principal Component Regression (PCR)	Regression analysis technique based on PCA by regressing the dependent variables on a set of independent variables based on a standard linear regression model, but uses PCA for estimating the unknown regression coefficients in the model.

Figure captions

Figure 1. Existing gas-detection philosophies versus our developed multivariable gas sensors. The gas cross-sensitivity problem of modern conventional sensors (A) originates from their design principles based on a single output of a sensor (B). High performance capabilities of traditional analytical instruments (C) are provided by their several independent outputs (D). Multivariable sensors also form independent variables in sensor response (D) but with reduced size and power, for example by using bio-inspired photonic nanostructures (E).

Figure 2. Schematic of our optimization of performance of multivariable sensors by refining the material, structural, and excitation characteristics of the sensor system thought the iterative multivariate ("machine learning", ML) analysis of system performance in each iteration.

Figure 3. Examples of fabricated bio-inspired photonic 3-D nanostructures for detection of non-condensable gases at high temperature. Nanostructure with gold nanoparticles (A) before and (B) after capping with a CeO_2 layer, respectively. (C) Cross sectional image and (D) Energy Dispersive X-Ray Spectroscopy mapping of Ce, Au, and O shown by different false colors. (E) Improved fabrication process of the nanostructure design shown in (C) by providing larger opening regions for horizontal lamella. (F) Nanostructure with gold nanoparticles inside the gaps between lamella.

Figure 4. Gas-response testing of fabricated bio-inspired photonic 3-D nanostructures. (A, B) Examples of prepared samples. (C) Built-in-house gas flow cell with an integrated heater and a

fiber-optic port for testing of sensing nanostructures for SOFC applications. The fiber-optic port was designed to illuminate the sensing nanostructure at 45^{o} angle.

Figure 5. Visual and machine learning analysis of spectral differences of response of a bare natural *Morpho* nanostructure to three diverse vapors with changing illumination angle of 20^{o}, 40^{o}, and 60^{o}. (A-C) Differential reflectance $\Delta R(\lambda)$ spectra from vapors (1 – 3) water, chloroform, and dimethylformamide at three angles; all vapors at 0.5 P/P_0. (D) PCA scores plot of PC1 and PC2 of nanostructure responses to vapors 1 – 3 at three angles. Highlighted with red, green, and blue lines are the increasing angles of the arcs between the responses to vapors 1 – 3 as a function of illumination angle.

Figure 6. Results of FDTD simulations of effects of the illumination angle on the gas-selectivity of a 3-D four-lamella sensing nanostructure. Effects of illumination angles of (A) 0^{o}, (B) 45^{o}, and (C) 60^{o}: Top graphs are the planar electromagnetic fields that interact with the 3-D sensing nanostructure at different angles. Shown in every graph is the resulting electric field amplitude normalized by the excitation electric field amplitude. Middle graphs are differential reflectance $\Delta R(\lambda)$ spectra. The spectral results are the ratio of the received optical power at the monitor plane to the optical power of the excitation wave and normalized using eq. 1. Bottom graphs are PCA scores plots of the first three PCs from four lamella (1-4) interacting with different vapors. (D) Contributions of PC1, PC2, and PC3 to the developed PCA models for different illumination angles. For these simulations we used vapors of four model solvents with refractive index n = 1.3, 1.4, 1.5, and 1.6 and their three vapor concentrations being related to condensed liquid layers of thickness d = 5, 10, and 15 nm formed on the nanostructure.

Figure 7. $\Delta R(\lambda)$ spectra of *Morpho* butterfly nanostructures to ten vapors. (A) Bare and (B) Fluorosilane-functionalized *Morpho* butterfly nanostructures. Vapors (at 0.22 P/P_0): (1) water; (2) methanol; (3) ethanol; (4) 1-propanol; (5) 1-butanol; (6) 1-pentanol; (7) 1- hexanol; (8) 1-heptanol; (9) 1-octanol; (10) 1-nonanol. Blank gas is (0).

Figure 8. Dynamic responses of *Morpho* butterfly nanostructure to ten vapors with replicate (n = 2) responses. (A) Bare and (B) Fluorosilane-functionalized *Morpho* butterfly nanostructures. Vapors: (1) water; (2) methanol; (3) ethanol; (4) 1-propanol; (5) 1-butanol; (6) 1-pentanol; (7) 1-hexanol; (8) 1-heptanol; (9) 1-octanol; (10) 1-nonanol. Blank gas is (0). Each vapor was presented to the nanostructures at four concentrations of 0.09, 0.13, 0.18, and 0.22 P/P_0. A hydration step (red arrows) between switching to different vapors was used to speed up the recovery of the wing sample to its baseline and was done by exposing the sample to water vapor at 0.35 P/P_0. (C) Zoomed-in regions from (A and B) for comparison of sensitivity to vapors 4 to 10 of the *Morpho* butterfly nanostructure before (blue lines) and after (green lines) functionalization with trimethoxy(nonafluorohexyl)silane.

Figure 9. PCA scores plots of the first three principal components from spectral responses $\Delta R(\lambda)$ of *Morpho* butterfly nanostructures to ten vapors. (A) Bare and (B) Fluorosilane-functionalized *Morpho* butterfly nanostructures. Vapors: (1) water; (2) methanol; (3) ethanol; (4) 1-propanol; (5) 1-butanol; (6) 1-pentanol; (7) 1- hexanol; (8) 1-heptanol; (9) 1-octanol; (10) 1-nonanol, with four concentrations of each vapor. Each vapor was presented to the nanostructures at four concentrations of 0.09, 0.13, 0.18, and 0.22 P/P_0 labeled as 1 – 4. For statistics we used two data points per concentration of each vapor and the blank.

Figure 10. Differential reflectance ΔR(λ) spectra of the fabricated photonic 3-D nanostructure upon exposures to gases of interest. (A) H_2 and (B) CO. Gas concentrations: H_2 at 4 %, 8 %, and 11%; CO at 6 %, 13 %, and 19%.

Figure 11. Dynamic responses of the fabricated photonic 3-D nanostructure to H_2 and CO with replicate (n = 2) responses. (A-D) Responses at ≈ 500 nm, 600 nm, 800 nm, and 900 nm, respectively. Gas concentrations: H_2 at 4 %, 8 %, and 11%; CO at 6 %, 13 %, and 19%.

Figure 12. Scores plot of the developed PCA model based on measurements of responses of the fabricated photonic 3-D nanostructure to H_2 and CO gases. Gas concentrations: H_2 at 4 %, 8%, and 11%; CO at 6 %, 13 %, and 19%. For statistics we used two data points per concentration of both gases and the blank.

Figure 13. Differential reflectance ΔR(λ) spectra of the fabricated photonic 3-D nanostructure with different size gold nanoparticles upon exposures to different gases. (A,B) Responses to H_2 and CO gases of interest, respectively. (C) Responses to three interference gases such as CH_4, CO_2, and H_2O (labeled as Int 1, 2, and 3, respectively). Concentrations of H_2 and CO gases were 12.5 %, 25 %, and 37.5 %. The CO_2 and CH_4 interferents were at 37.5%. The H_2O (water vapor) interferent was at 30 % RH.

Figure 14. Dynamic response of the fabricated photonic 3-D nanostructure to H_2 and CO gases of interest and three interference gases (CH_4, CO_2, and H_2O (Int 1 - 3). Shown is response at 950 nm. Concentrations of H_2 and CO gases were 12.5 %, 25 %, and 37.5%. The CO_2 and CH_4 interferents were at 37.5 %. The H_2O (water vapor) interferent was at 30% RH.

Figure 15. Scores plots of the developed PCA model based on measurements of the responses of the fabricated photonic 3-D nanostructure to a blank, three concentrations of H_2 and CO gases of interest and one concentration of three interference gases CH_4, CO_2, and H_2O (Int 1 - 3). (A) Plot of PC1 vs. PC2 vs. PC3. (A) Plot of PC1 vs. PC2 vs. PC4. Concentrations of H_2 and CO gases: 12.5 %, 25 %, and 37.5%. The CO_2 and CH_4 interferents: at 37.5 %. The H_2O vapor interferent: at 30 % RH. For statistics we used two data points per concentration of all gases and the blank.

References

1. T. R. Fadel, D. F. Farrell, L. E. Friedersdorf, M. H. Griep, M. D. Hoover, M. A. Meador and M. Meyyappan, *ACS Sens.*, 2016, 207-216.
2. J. Janata, *Principles of Chemical Sensors*, Springer, New York, NY, 2 edn., 2009.
3. A. Lewis and P. Edwards, *Nature*, 2016, **535**, 29-31.
4. R. G. Cooks, Z. Ouyang, Z. Takats and J. M. Wiseman, *Science*, 2006, **311**, 1566-1570.
5. D. T. Allen, V. M. Torres, J. Thomas, D. W. Sullivan, M. Harrison, A. Hendler, S. C. Herndon, C. E. Kolb, M. P. Fraser, A. D. Hill, B. K. Lamb, J. Miskimins, R. F. Sawyer and J. H. Seinfeldi, *Proc. Natl. Acad. Sci. U.S.A.*, 2013, **110**, 17768-17773.
6. L. Zhang, G. Tian, J. Li and B. Yu, *Appl. Spectrosc.*, 2014, **68**, 1095-1107.
7. J. Wang, N. Nuñovero, R. Nidetz, S. J. Peterson, B. M. Brookover, W. H. Steinecker and E. T. Zellers, *Anal. Chem.*, 2019, **91**, 4747-4754.
8. D. Janasek, J. Franzke and A. Manz, *Nature*, 2006, **442**, 374-380.
9. R. A. Potyrailo and W. G. Morris, *Anal. Chem.*, 2007, **79**, 45-51.
10. R. A. Potyrailo, W. G. Morris, T. Sivavec, H. W. Tomlinson, S. Klensmeden and K. Lindh, *Wirel. Commun. Mob. Comput.*, 2009, **9**, 1318-1330.
11. R. A. Potyrailo, C. Surman, S. Go, Y. Lee, T. Sivavec and W. G. Morris, *J. Appl. Phys.*, 2009, **106**, 124902.
12. R. A. Potyrailo, C. Surman, W. G. Morris, S. Go, Y. Lee, J. A. Cella and K. S. Chichak, *IEEE Int. Conf. on RFID, IEEE RFID*, 2010, 22-28.
13. R. A. Potyrailo, A. Burns, C. Surman, D. J. Lee and E. McGinniss, *Analyst*, 2012, **137**, 2777-2781.
14. R. A. Potyrailo, N. Nagraj, C. Surman, H. Boudries, H. Lai, J. M. Slocik, N. Kelley-Loughnane and R. R. Naik, *Trends Anal. Chem.*, 2012, **40**, 133-145.
15. N. Nagraj, J. M. Slocik, D. M. Phillips, N. Kelley-Loughnane, R. R. Naik and R. A. Potyrailo, *Analyst*, 2013, **138**, 4334-4339.
16. R. A. Potyrailo, M. Larsen and O. Riccobono, *Angew. Chem. Int. Ed.*, 2013, **52**, 10360-10364.
17. R. A. Potyrailo and R. R. Naik, *Annu. Rev. Mater. Res.*, 2013, **43**, 307–334.
18. R. A. Potyrailo, *Chem. Rev.*, 2016, **116**, 11877–11923.
19. K. Persaud and G. Dodd, *Nature*, 1982, **299**, 352-355.
20. S. H. Lim, L. Feng, J. W. Kemling, C. J. Musto and K. S. Suslick, *Nat. Chem.*, 2009, 562-567.

21. G. Peng, U. Tisch, O. Adams, M. Hakim, N. Shehada, Y. Y. Broza, S. Billan, R. Abdah-Bortnyak, A. Kuten and H. Haick, *Nat. Nanotechnol.*, 2009, **4**, 669-673.
22. A. Lichtenstein, E. Havivi, R. Shacham, E. Hahamy, R. Leibovich, A. Pevzner, V. Krivitsky, G. Davivi, I. Presman, R. Elnathan, Y. Engel, E. Flaxer and F. Patolsky, *Nat. Commun.*, 2014, **5**, art. no. 4195.
23. R. Beccherelli, E. Zampetti, S. Pantalei, M. Bernabei and K. C. Persaud, *Sens. Actuators B*, 2010, **146**, 446-452.
24. M. Bernabei, K. C. Persaud, S. Pantalei, E. Zampetti and R. Beccherelli, *IEEE Sensors J.*, 2012, **12**, 3174-3183.
25. S. Marco, A. Gutiérrez-Gálvez, A. Lansner, D. Martinez, J. P. Rospars, R. Beccherelli, A. Perera, T. C. Pearce, P. F. M. J. Verschure and K. Persaud, *Microsys. Technol.*, 2014, **20**, 729-742.
26. M. E. H. Amrani, R. M. Dowdeswell, P. A. Payne and K. C. Persaud, *Sens. Actuators, B*, 1997, **44**, 512-516.
27. L. Torsi, A. Dodabalapur, L. Sabbatini and P. G. Zambonin, *Sens. Actuators, B*, 2000, **67**, 312-316.
28. A. Hierlemann and R. Gutierrez-Osuna, *Chem. Rev.*, 2008, **108**, 563-613.
29. M. W. K. Nomani, D. Kersey, J. James, D. Diwan, T. Vogt, R. A. Webb and G. Koley, *Sens. Actuators, B*, 2011, **160**, 251-259.
30. A. Schütze, A. Gramm and T. Rühl, *IEEE Sensors J.*, 2004, **4**, 857-863.
31. N. C. Speller, N. Siraj, B. P. Regmi, H. Marzoughi, C. Neal and I. M. Warner, *Anal. Chem.*, 2015, **87**, 5156-5166.
32. R. A. Potyrailo, H. Ghiradella, A. Vertiatchikh, K. Dovidenko, J. R. Cournoyer and E. Olson, *Nat. Photonics*, 2007, **1**, 123-128.
33. R. A. Potyrailo, T. Starkey, P. Vukusic, H. Ghiradella, M. Vasudev, T. Bunning, R. R. Naik, Z. Tang, M. Larsen, T. Deng, S. Zhong, M. Palacios, J. C. Grande, G. Zorn, G. Goddard and S. Zalubovsky, *Proc. Natl. Acad. Sci. U.S.A.*, 2013, **110**, 15567–15572.
34. R. A. Potyrailo, R. K. Bonam, J. G. Hartley, T. A. Starkey, P. Vukusic, M. Vasudev, T. Bunning, R. R. Naik, Z. Tang, M. Palacios, M. Larsen, L. A. Le Tarte, J. C. Grande, T. Deng and S. Zhong, *Nat. Commun.*, 2015, **6**, 7959.
35. D. Bhattacharyya and R. Rengaswamy, *Ind. Eng. Chem. Res.*, 2009, **48**, 6068-6086.
36. A. Gelen and T. Yalcinoz, *Fuel Cells*, 2015, **15**, 571-579.
37. S. Akbar, P. Dutta and C. Lee, *Int. J. Appl. Ceram. Technol.*, 2006, **3**, 302-311.
38. A. Heinzel, B. Vogel and P. Hübner, *J. Power Sources*, 2002, **105**, 202-207.
39. A. Williams and L. D. Williams, *Contrivance for automatically detecting the presence of certain gases and vapors*, US Patent 1,143,473, 1915.
40. G. Ljunggren, *Means for and method of detecting the presence of carbon monoxide*, US Patent 1,891,429, 1932.
41. H. Kott, *Humidity measuring device*, US Patent 2,047,638, 1936.
42. A. R. Baker, *Apparatus for detecting combustible gases having an electrically conductive member enveloped in a refractory material*, US Patent 3,092,799, 1963.
43. N. Taguchi, *Method for making a gas-sensing element*, US Patent 3,625,756, 1971.
44. J. E. Meinhard, *Electronic Olfactory Detector Having Organic Semiconductor Barrier Layer Structure*, US Patent 3,428,892, 1969.
45. M. I. Jordan and T. M. Mitchell, *Science*, 2015, **349**, 255-260.
46. W. Wei, O. Ramalho, L. Malingre, S. Sivanantham, J. C. Little and C. Mandin, *Indoor Air*, 2019.
47. R. A. Potyrailo, *Chem. Soc. Rev.*, 2017, **46**, 5311-5346.
48. R. A. Potyrailo, *Tutorial: Multivariable gas sensors: delivering needed selectivity and stability for modern applications*, IEEE SENSORS, New Delhi, India, October 28-31, 2018.
49. F. Josse, R. Lukas, R. Zhou, S. Schneider and D. Everhart, *Sens. Actuators, B*, 1996, **35-36**, 363-369.
50. R. D. Yang, B. Fruhberger, J. Park and A. C. Kummel, *Appl. Phys. Lett.*, 2006, **88**, 074104.

51. G. Shuster, S. Baltianski, Y. Tsur and H. Haick, *J. Phys. Chem. Lett.*, 2011, **2**, 1912-1916.
52. W. T. Chen, K. M. E. Stewart, R. R. Mansour and A. Penlidis, *Sens. Actuators, A*, 2015, **230**, 63-73.
53. Y. Kunugi, K. Nigorikawa, Y. Harima and K. Yamashita, *J. Chem. Soc.: Chem. Comm.*, 1994, 873-874.
54. A. F. Holloway, A. Nabok, M. Thompson, A. K. Ray and T. Wilkop, *Sens. Actuators, B*, 2004, **99**, 355-360.
55. B. P. Regmi, J. Monk, B. El-Zahab, S. Das, F. R. Hung, D. J. Hayes and I. M. Warner, *J. Mater. Chem. C*, 2012, **22**, 13732-13741.
56. C. Bur, M. Bastuck, D. Puglisi, A. Schütze, A. Lloyd Spetz and M. Andersson, *Sens. Actuators, B*, 2015, **214**, 225–233.
57. N. Karker, G. Dharmalingam and M. A. Carpenter, *ACS Nano*, 2014, **8**, 10953-10962.
58. R. Ionescu, *Sens. Actuators, B*, 1998, **B48**, 392-394.
59. C. J. Oton, L. Pancheri, Z. Gaburro, L. Pavesi, C. Baratto, G. Faglia and G. Sberveglieri, *Phys. Status Solidi A*, 2003, **197**, 523-527.
60. S. I. Lysenko, E. B. Kaganovich, I. M. Kizyak and B. A. Snopok, *Sensor Lett.*, 2005, **3**, 117-125.
61. I. S. Chen, M. Stawasz, S. K. DiMascio, J. J. Welch, J. W. Neuner, P. S. H. Chen and F. DiMeo Jr, *Appl. Phys. Lett.*, 2005, **86**, 1-3.
62. M. Qazi, T. Vogt and G. Koley, *Appl. Phys. Lett.*, 2008, **92**, 103120.
63. A. Loui, D. J. Sirbuly, S. Elhadj, S. K. McCall, B. R. Hart and T. V. Ratto, *Sens. Actuators, A*, 2010, **159**, 58-63.
64. L. Wang and J. S. Swensen, *Sens. Actuators, B*, 2012, **174**, 366-372.
65. R. A. Potyrailo, Z. Ding, M. D. Butts, S. E. Genovese and T. Deng, *IEEE Sensors J.*, 2008, **8**, 815-822.
66. J. E. Royer, E. D. Kappe, C. Zhang, D. T. Martin, W. C. Trogler and A. C. Kummel, *J. Phys. Chem. C*, 2012, **116**, 24566-24572.
67. B. Wang, J. C. Cancilla, J. S. Torrecilla and H. Haick, *Nano Lett.*, 2014, **14**, 933-938.
68. N. A. Joy, M. I. Nandasiri, P. H. Rogers, W. Jiang, T. Varga, S. V. N. T. Kuchibhatla, S. Thevuthasan and M. A. Carpenter, *Anal. Chem.*, 2012, **84**, 5025-5034.
69. N. A. Joy, P. H. Rogers, M. I. Nandasiri, S. Thevuthasan and M. A. Carpenter, *Anal. Chem.*, 2012, **84**, 10437-10444.
70. X. Yang, Z. Peng, H. Zuo, T. Shi and G. Liao, *Sens. Actuators, A*, 2011, **167**, 367-373.
71. G. Piszter, K. Kertész, Z. Vértesy, Z. Bálint and L. P. Biró, *Opt. Express*, 2014, **22**, 22649-22660.
72. G. Piszter, K. Kertész, Z. Vértesy, Z. Bálint and L. P. Biró, *Mater. Today Proc.*, 2014, **1**, 216-220.
73. T. Jiang, Z. Peng, W. Wu, T. Shi and G. Liao, *Sens. Actuators, A*, 2014, **213**, 63-69.
74. G. Piszter, K. Kertész, Z. Bálint and L. P. Biró, *Sensors*, 2016, **16**, 1446.
75. J. D. Kittle, B. P. Fisher, A. J. Esparza, A. M. Morey and S. T. Iacono, *ACS Omega*, 2017, **2**, 8301-8307.
76. K. Kertész, G. Piszter, Z. Bálint and L. P. Biró, *Sensors*, 2018, **18**, 4282.
77. G. Piszter, K. Kertész, Z. Bálint and L. P. Biró, *Sensors*, 2019, **19**, 3058.
78. J. Kittle, B. Fisher, C. Kunselman, A. Morey and A. Abel, *Sensors*, 2020, **20**, 157.
79. K. R. Phillips, G. T. England, S. Sunny, E. Shirman, T. Shirman, N. Vogel and J. Aizenberg, *Chem. Soc. Rev.*, 2016, **45**, 281-322.
80. A. G. Dumanli and T. Savin, *Chem. Soc. Rev.*, 2016, **45**, 6698-6724.
81. Q. Li, Q. Zeng, L. Shi, X. Zhang and K.-Q. Zhang, *J. Mater. Chem. C*, 2016, **4**, 1752-1763.
82. Y. Y. Diao, X. Y. Liu, G. W. Toh, L. Shi and J. Zi, *Adv. Funct. Mater.*, 2013, **23**, 5373-5380.
83. Z. Xie, K. Cao, Y. Zhao, L. Bai, H. Gu, H. Xu and Z. Z. Gu, *Adv. Mater.*, 2014, **26**, 2413-2418.
84. Y. Zhang, J. Qiu, R. Hu, P. Li, L. Gao, L. Heng, B. Z. Tang and L. Jiang, *Phys. Chem. Chem. Phys.*, 2015, **17**, 9651-9658.
85. P. Ganter, K. Szendrei and B. V. Lotsch, *Adv. Mater.*, 2016, **28**, 7436-7442.

86. Y.-L. Ko, H.-P. Tsai, K.-Y. Lin, Y.-C. Chen and H. Yang, *J. Colloid Interface Sci.*, 2017, **487**, 360-369.
87. J. Gao, T. Gao and M. J. Sailor, *Appl. Phys. Lett.*, 2000, **77**, 901-903.
88. K. P. Raymond, I. B. Burgess, M. H. Kinney, M. Lončar and J. Aizenberg, *Lab Chip*, 2012, **12**, 3666-3669.
89. H. Zhang, L. Lin, D. Liu, Q. Chen and J. Wu, *Anal. Chim. Acta*, 2017, **953**, 71-78.
90. S. R. Mouchet, T. Tabarrant, S. Lucas, B.-L. Su, P. Vukusic and O. Deparis, *Opt. Express*, 2016, **24**, 12267-12280.
91. J. Rasson, O. Poncelet, S. R. Mouchet, O. Deparis and L. A. Francis, *Mater. Today Proc.*, 2017, **4**, 5006-5012.
92. O. Poncelet, G. Tallier, S. R. Mouchet, A. Crahay, J. Rasson, R. Kotipalli, O. Deparis and L. A. Francis, *Bioinspir. Biomim.*, 2016, **11**, 036011.
93. G. I. Márk, K. Kertész, G. Piszter, Z. Bálint and L. P. Biró, *Nanomaterials*, 2019, **9**, 759.
94. R. A. Potyrailo, N. Karker, M. A. Carpenter and A. Minnick, *J. Opt.*, 2018, **20**, 024006.
95. R. Potyrailo, V. Srivastava, J. Brewer, C. Henderson, B. Scherer, M. Nayeri, A. Shapiro, M. Carpenter, N. Karker, N. Houlihan, V. Vulcano Rossi and L. Banu, *Highly Selective and Stable Multivariable Gas Sensors for Enhanced Robustness and Reliability of SOFC Operation*, 19th Annual SOFC Project Review Meeting, Washington, D.C., June 13-15, https://www.netl.doe.gov/events/conference-proceedings/2018/19th-annual-solid-oxide-fuel-cell-sofc-project-review-meeting, 2018.
96. R. Potyrailo, J. Brewer, R. St-pierre, B. Scherer, M. Nayeri, C. Collazo-Davila, A. Shapiro, M. Carpenter, N. Houlihan, V. Vulcano Rossi and L. Banu, *Multi-Gas Sensors for Enhanced Reliability of SOFC Operation*, 20th Annual SOFC Project Review Meeting, Crystal City, Virginia, April 29 - May 01, https://netl.doe.gov/sites/default/files/2019-05/2019%20SOFC%20Proceedings/FE27-GE%20NETL%20FE0031653%20annual%20review%20WEB%20Version.pdf, 2019.
97. R. A. Potyrailo, J. Brewer, B. Scherer, V. Srivastava, M. Nayeri, C. Henderson, C. Collazo-Davila, M. A. Carpenter, N. Houlihan, V. Vulcano Rossi and A. Shapiro, *ECS Transactions*, 2019, **91**, 319-328.
98. J. D. Ingle, Jr. and S. R. Crouch, *Spectrochemical Analysis*, Prentice Hall, Englewood Cliffs, NJ, 1988.
99. R. A. Potyrailo, C. Surman, N. N. Nagraj and A. Burns, *Chem. Rev.*, 2011, **111**, 7315–7354.
100. R. A. Potyrailo, *Tutorial: Multivariable sensors for selective and stable gas monitoring*, IEEE International Symposium on Olfaction and Electronic Nose (ISOEN), Fukuoka, Japan, May 26-29, 2019.
101. B. A. Snopok and I. V. Kruglenko, *Thin Solid Films*, 2002, **418**, 21-41.
102. J. Burlachenko, I. Kruglenko, B. Snopok and K. Persaud, *Trends Anal. Chem.*, 2016, **82**, 222-236.
103. N. Houlihan, N. Karker, R. A. Potyrailo and M. Carpenter, *ACS Sens.*, 2018, **3**, 2684-2692.
104. M. A. Steindorfer, V. Schmidt, M. Belegratis, B. Stadlober and J. R. Krenn, *Opt. Express*, 2012, **20**, 21485-21494.
105. J. He, N. S. Villa, Z. Luo, S. An, Q. Shen, P. Tao, C. Song, J. Wu, T. Deng and W. Shang, *RSC Adv.*, 2018, **8**, 32395-32400.
106. P. Raksrithong and K. Locharoenrat, *AIP Adv.*, 2019, **9**, 075311.
107. M. Calhoun, J. Sanchez, D. Olaya, M. Gershenson and V. Podzorov, *Nat. Mater.*, 2008, **7**, 84-89.
108. Z. Yang and X. Dou, *Adv. Funct. Mater.*, 2016, **26**, 2406-2425.
109. C.-F. Lu, S.-F. Liao, I.-F. Chen, C.-T. Chen, C.-Y. Chao and W.-F. Su, *ACS Appl. Electron. Mater.*, 2019, **1**, 1873-1880.

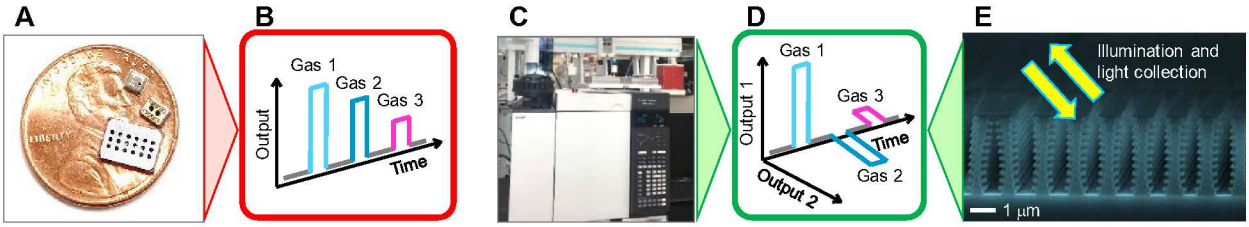

Figure 1.

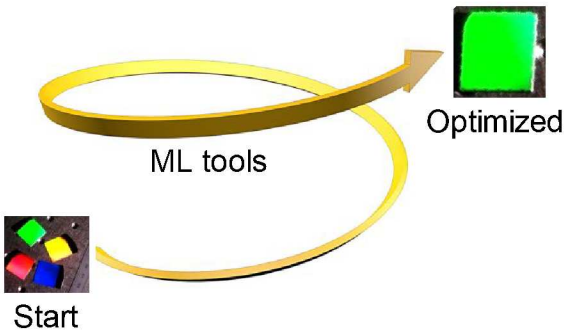

Figure 2.

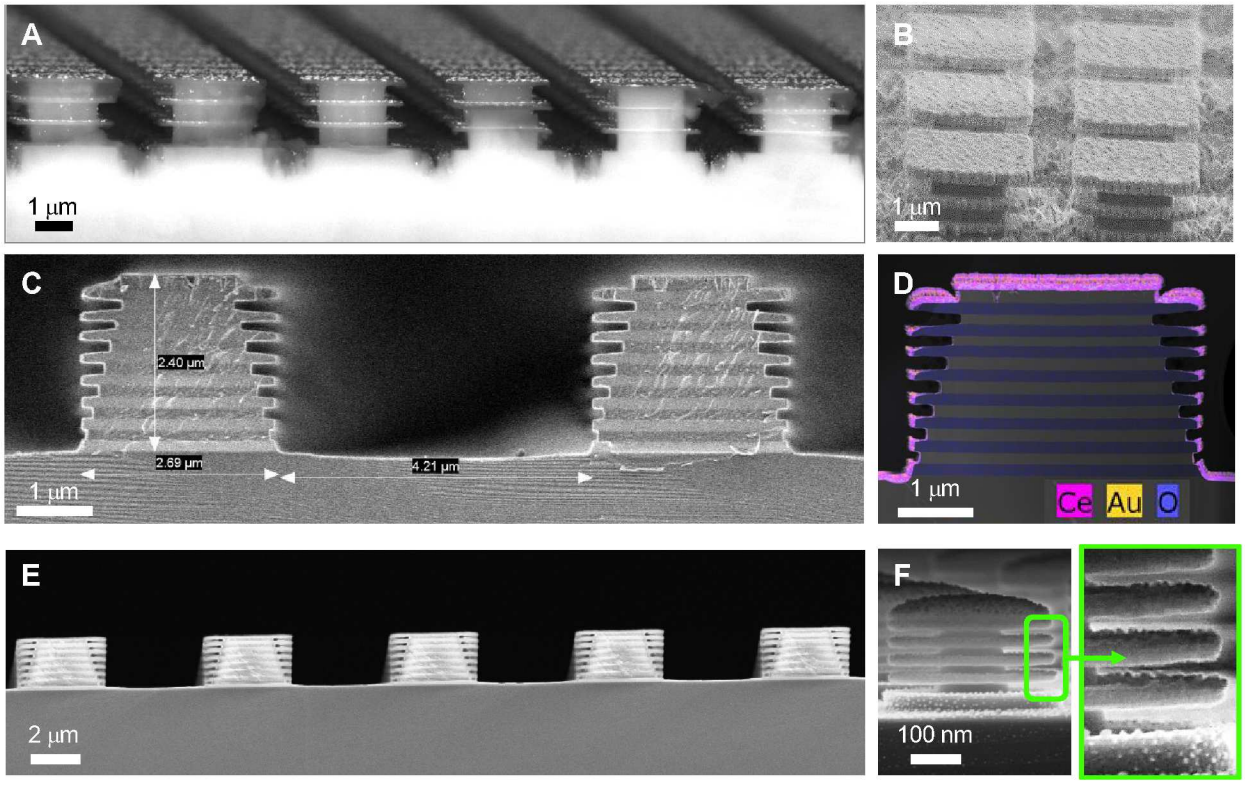

Figure 3.

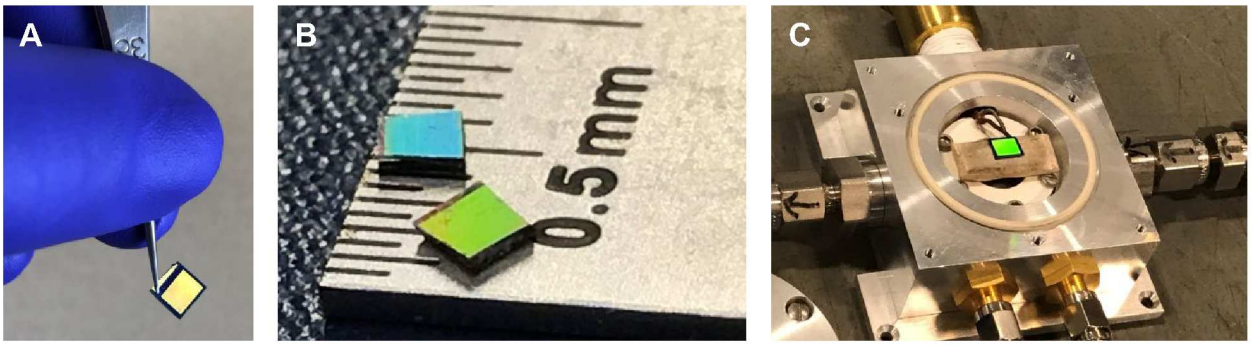

Figure 4.

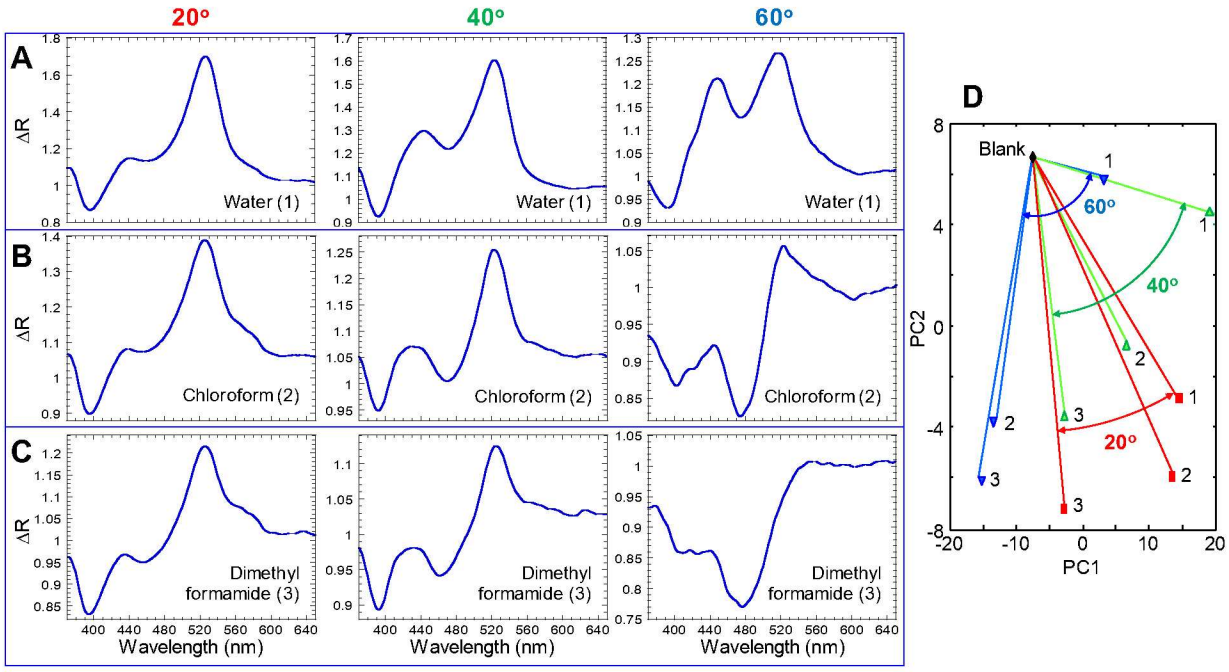

Figure 5.

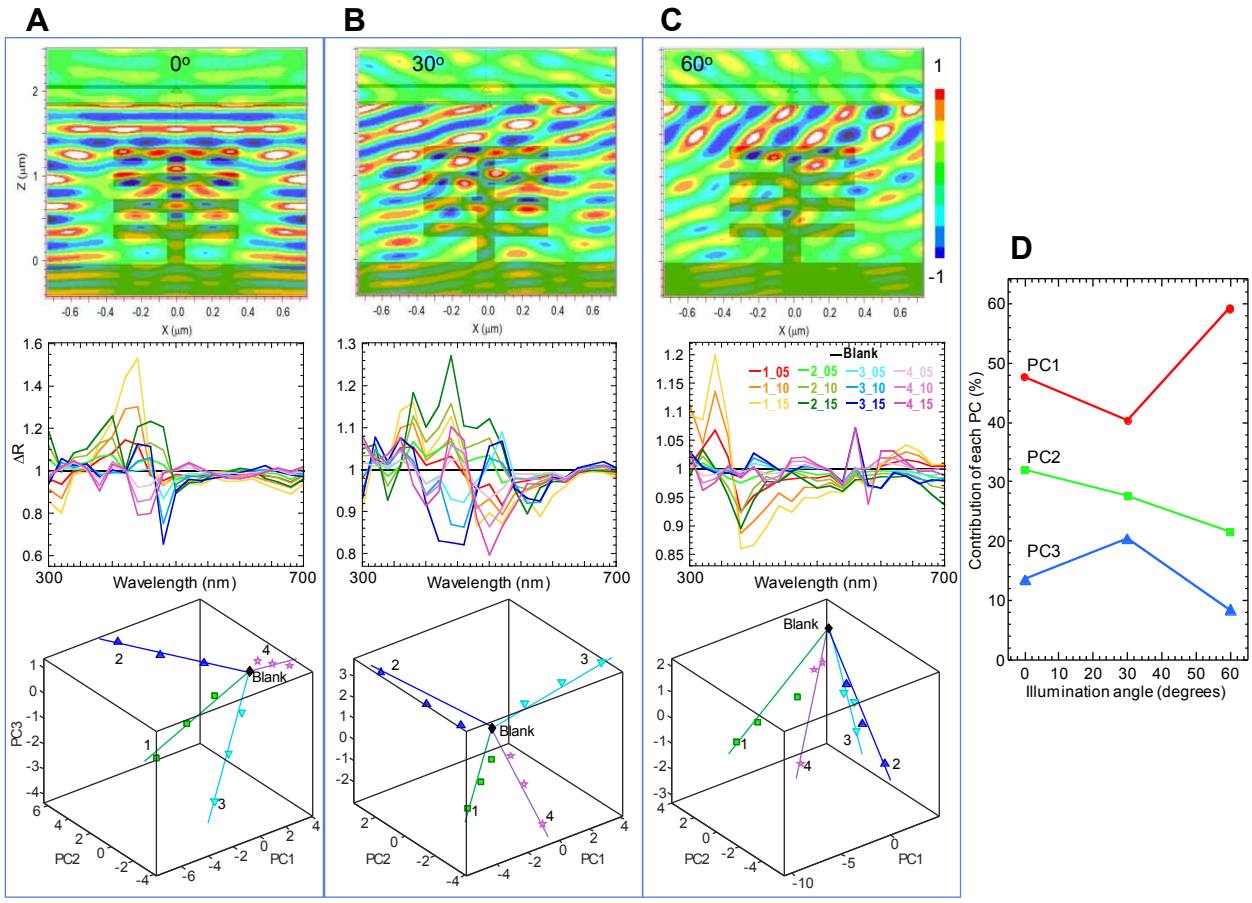

Figure 6.

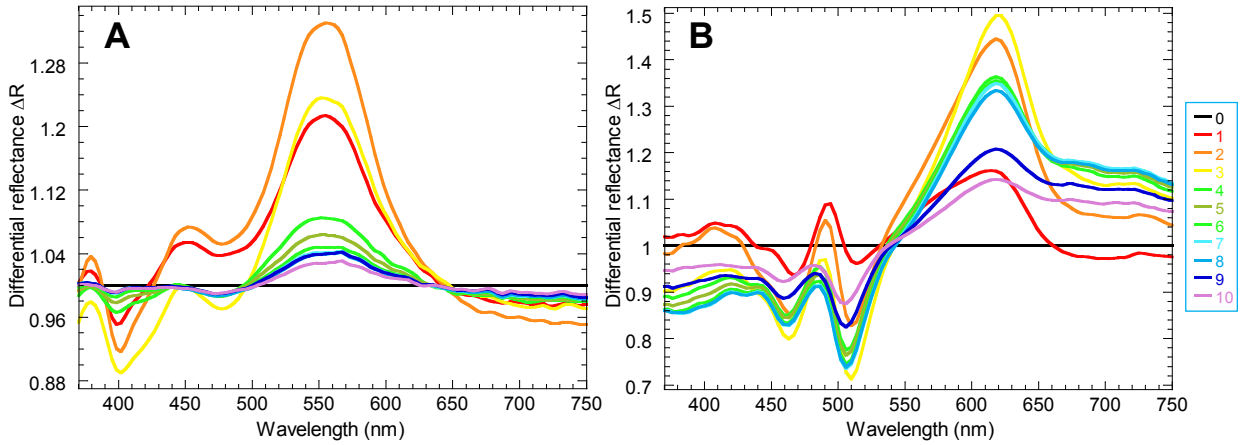

Figure 7.

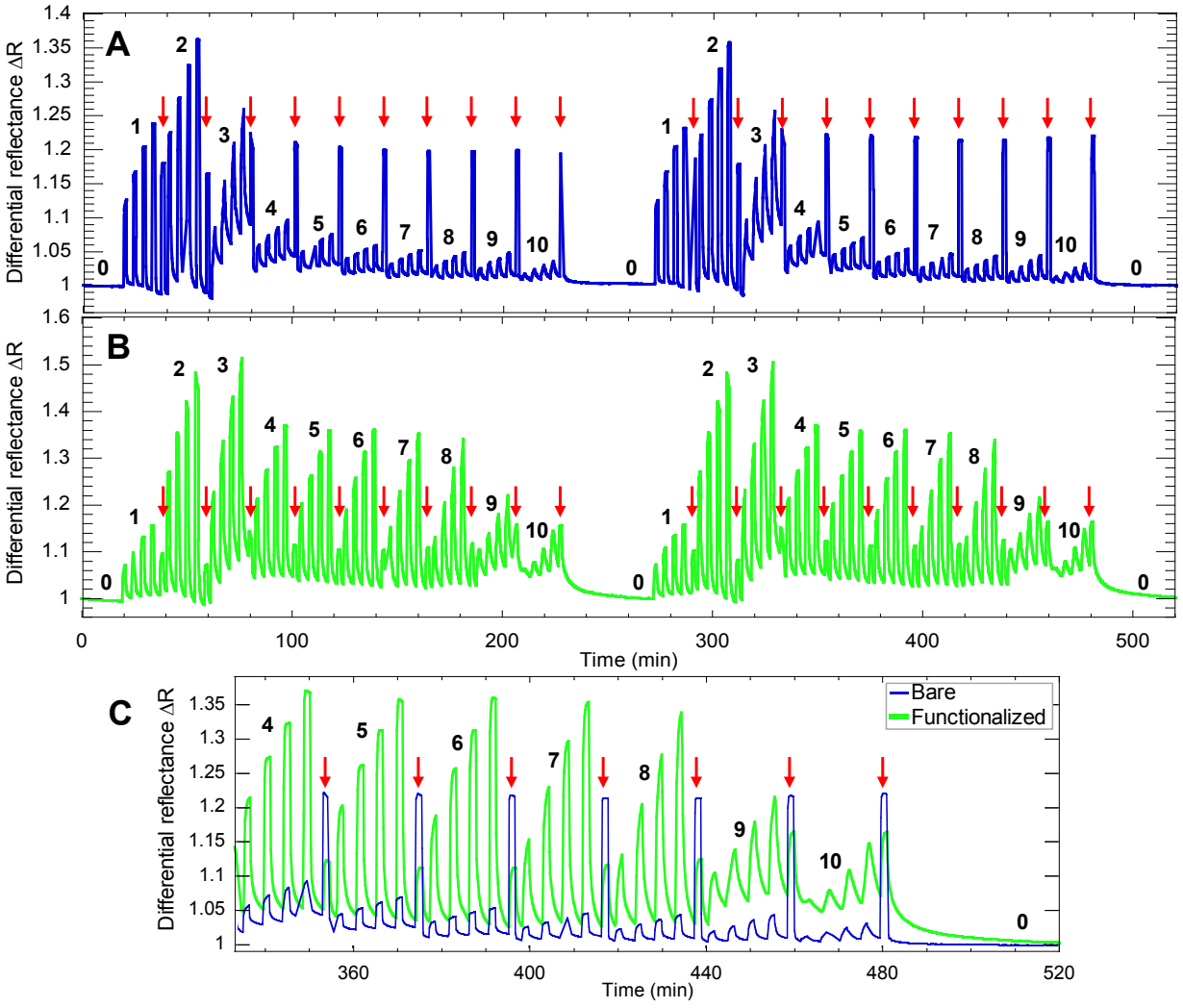
A
B
C
Differential reflectance ΔR
Time (min)
Bare
Functionalized

Figure 8.

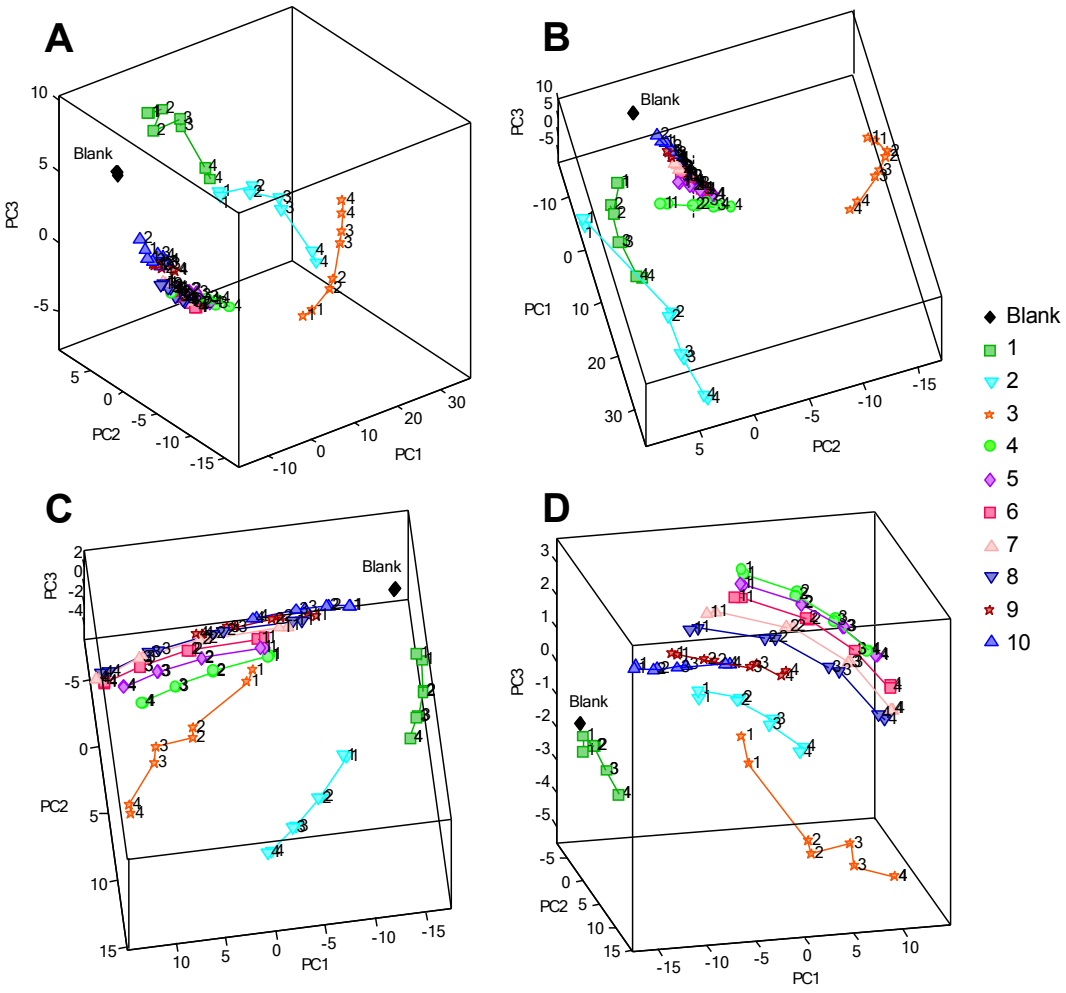

Figure 9.

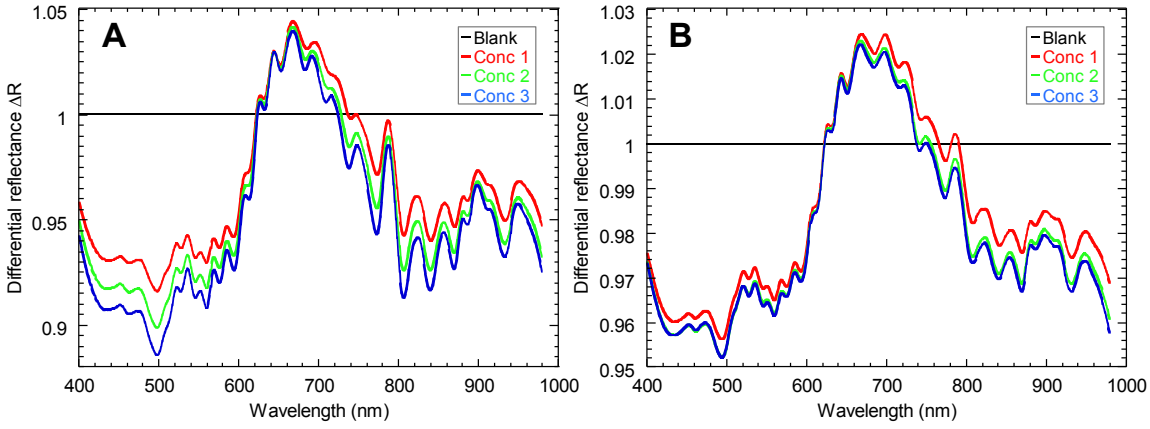

Figure 10.

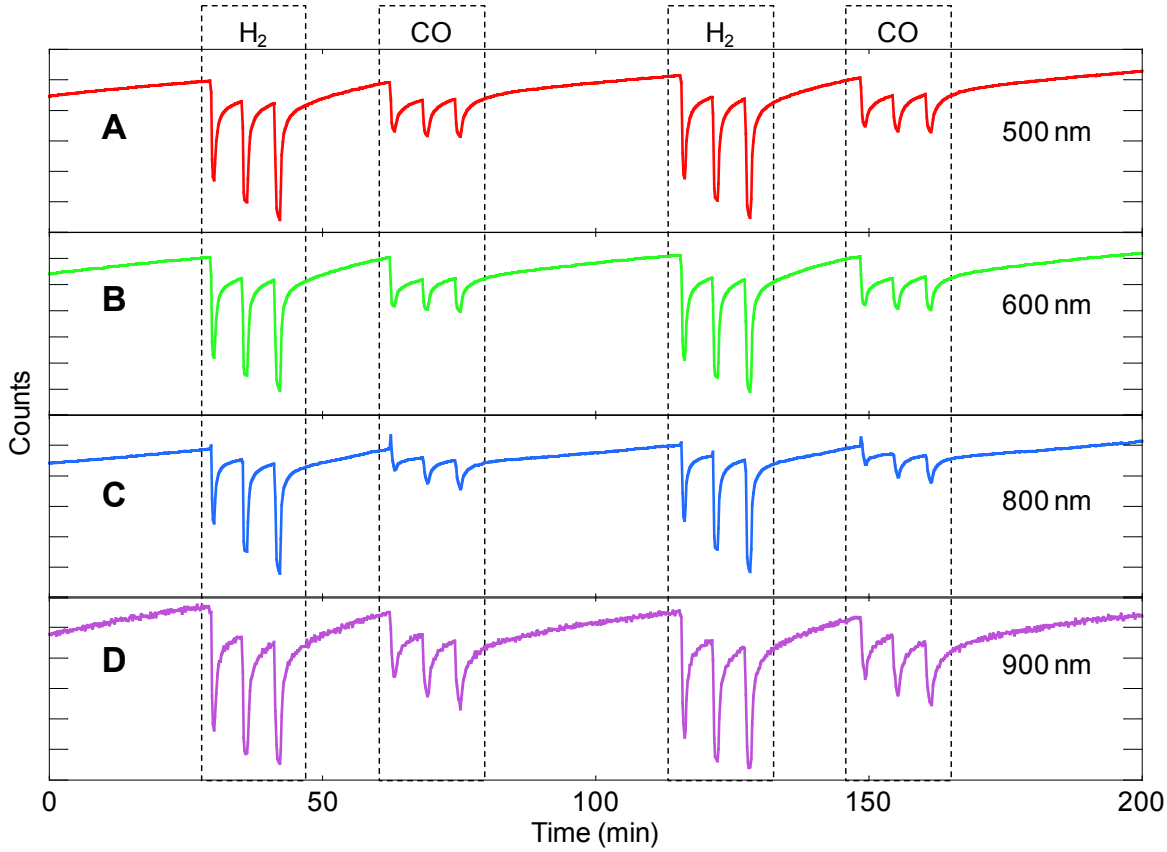

Figure 11.

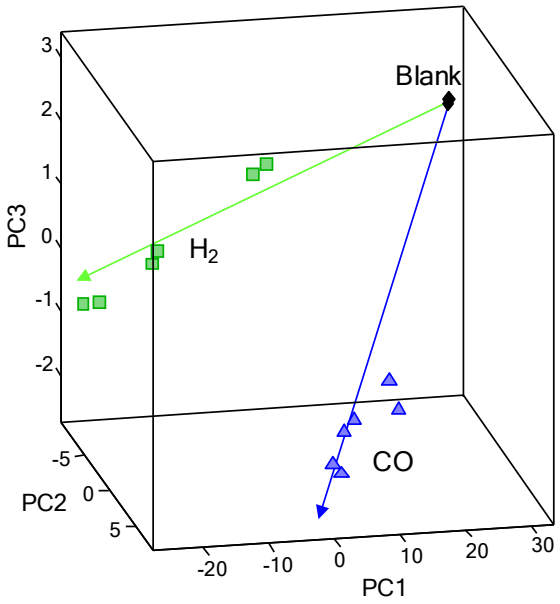

Figure 12.

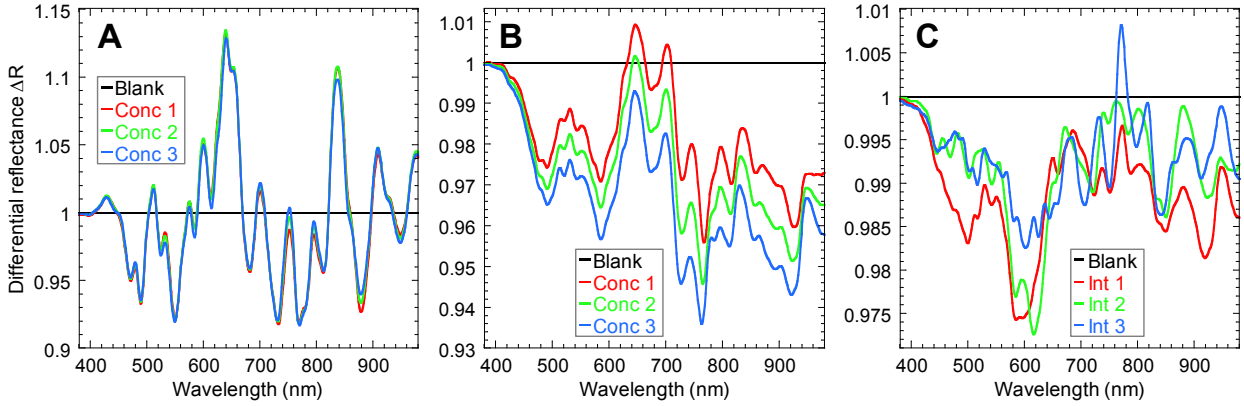

Figure 13.

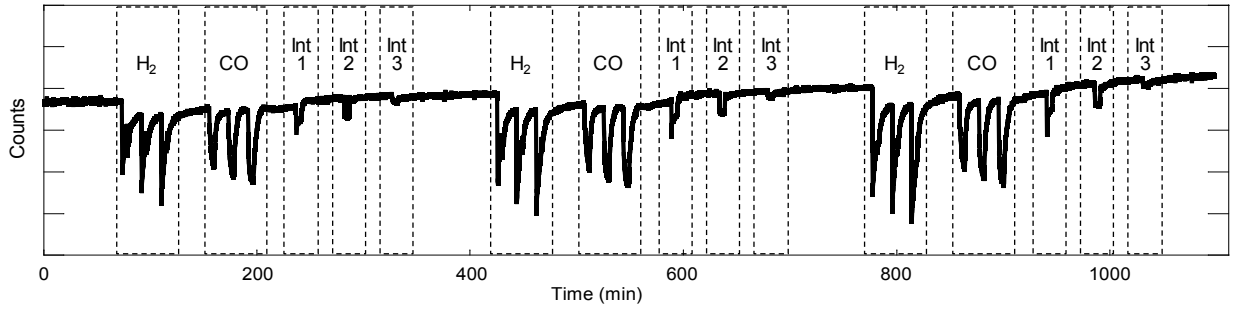

Figure 14.

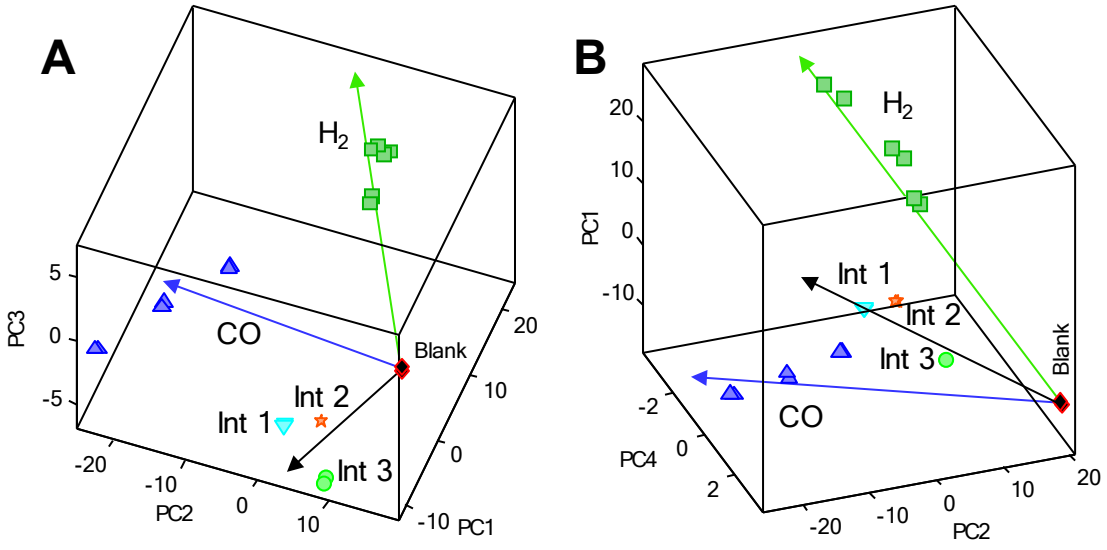

Figure 15.